1   **Calculation of the energetics of water incorporation in majorite garnet**

2   **Jeffrey S. Pigott[1*], Kate Wright[2], Julian D. Gale[2], and Wendy R. Panero[1]**

3   [1]School of Earth Sciences, Ohio State University, Columbus, OH, 43210, USA.

4   [2]Nanochemistry Research Institute, Department of Chemistry, Curtin University, PO Box

5   U1987, Perth, WA 6845, Australia.

6   *E-mail: pigott.2@osu.edu

7   **Abstract**

8   Interpretation of lateral variations in upper mantle seismic wave speeds requires

9   constraints on the relationship between elasticity and water concentration at high-pressure for all

10   major mantle minerals, including the garnet component. We have calculated the structure and

11   energetics of charge-balanced hydrogen substitution into tetragonal $MgSiO_3$ majorite up to $P =$

12   25 GPa using both classical atomistic simulations and complementary first-principles

13   calculations. At the pressure conditions of Earth's transition zone, hydroxyl groups are predicted

14   to be bound to Si vacancies as the hydrogarnet defect, $[V_{Si} + 4OH_O]^X$, at the Si2 tetrahedral site

15   or as the $[V_{Mg} + 2OH_O]^X$ defect at the octahedral Mg3 site. The hydrogarnet defect is more

16   favorable than the $[V_{Mg} + 2OH_O]^X$ defect by $0.8 - 1.4$ eV/H at 20 GPa. The presence of 0.4 wt%

17   Al_2O_3 substituted into the octahedral sites further increases the likelihood of the hydrogarnet

18   defect by 2.2-2.4 eV/H relative to the $[V_{Mg} + 2OH_O]^X$ defect at the Mg3 site. OH defects affect

19   the seismic ratio, $R = dlnV_s/dlnV_p$, in $MgSiO_3$ majorite ($\Delta R = 0.9 - 1.2$ at 20 GPa for 1400 ppm

20   wt H_2O) differently than ringwoodite at high pressure, yet may be indistinguishable from the

21   thermal $dlnV_s/dlnV_p$ for ringwoodite. The incorporation of 3.2 wt% Al_2O_3 also decreases $R(H_2O)$

22   by ~0.2-0.4. Therefore, to accurately estimate transition zone compositional and thermal

23   anomalies, hydrous majorite needs to be considered when interpreting seismic body wave

24   anomalies in the transition zone.

25   **Keywords**

26   Hydrous majorite, Defect mechanisms, Force field, Computer simulation, Density functional

27   theory

28   **Introduction**

29   The amount of water stored in deep crustal and mantle rocks is largely unconstrained, yet

30   may account for a quantity of water comparable to or in excess of the amount contained in the

31   present oceans (Hirschmann 2006). Water has a first-order effect on the compressibility and

32   deformation of the crust and mantle (e.g., Smyth et al. 2004; Xu et al. 2013) in addition to

33   melting temperature, electrical and thermal conductivity (e.g., Hirschmann 2006; Panero et al.

34   2013; Thomas et al. 2012). Since water is incorporated into the nominally anhydrous mineral

35   phases of Earth's mantle in the form of H defects (e.g., Wright 2006), a clear understanding of

36   the atomic scale behavior and substitution mechanism of hydrogen in high-pressure silicates is

37   critical to our knowledge of mantle processes.

38   Majorite, $(Mg,Fe)SiO_3$, is the high-pressure garnet phase stable at transition-zone depths

39   (410 – 660 km) and is the second most abundant phase after the high-pressure olivine

40   polymorphs, accounting for as much as 40 percent of the rock volume (Frost 2008). The defect-

41   free, tetragonal Mg-endmember garnet, majorite (space group $I4_1/a$), has a structure consisting of

42   3 unique tetrahedral sites (Si1, Si2, and Si3) each linked by corner oxygens to octahedral sites,

43   Mg3 and Si4, and two interstitial distorted dodecahedral sites, Mg1 and Mg2 (Figure 1) (Angel

44   et al. 1989). The 3 tetrahedral sites are distinguished from each other based on the occupancy of

45   the nearest neighbor octahedral sites. The Si1 tetrahedra are linked to Mg3 octahedra, the Si2

46   sites are linked to Si4 octahedra, and Si3 tetrahedra are linked to 2 Mg3 octahedra and 2 Si4

47   octahedra. The interstitial Mg1 dodecahedral site is more distorted than the Mg2 site.   There are

48   6 unique oxygen sites (Supplemental Data: Table S1). The O1 and O2 sites have the same

49   bonding environment but O1 is bonded to octahedral Mg and O2 is bonded to octahedral

50   silicon. The O3 and O4 sites are both doubly bonded to the Mg1 distorted cubic site. Finally, the

51   O5 and O6 sites are both involved in 2 cubic environments and 1 tetrahedra but O6 is bonded to

52   the octahedral Si and O5 is bonded to the Mg octahedra.

53   The dominant carriers of hydrogen in the transition zone are the high-pressure

54   polymorphs of $(Mg,Fe)_2SiO_4$ (olivine), wadsleyite and ringwoodite, which can incorporate

55   significant amounts of hydrogen (1-3 wt% H_2O) into their structures (e.g., Kohlstedt et al. 1996;

56   Smyth and Jacobsen 2006). Partitioning experiments in the MgO-SiO_2-H_2O system at transition

57   zone P-T conditions show that the olivine polymorphs (wadsleyite and ringwoodite) dissolve ~ 1

58   order of magnitude more than $MgSiO_3$ (majorite, clinoenstatite, akimotoite) (Bolfan-Casanova et

59   al. 2000) such that $D^{Mg2SiO4/MgSiO3} = \sim 10$.   Because the solubility of water in the olivine

60   polymorphs decreases with temperature and the partitioning of water between wadsleyite and

61   ringwoodite may be close to $D^{wad/ring} = 1$ at high temperature (Bolfan-Casanova 2005), majorite

62   solubility and partitioning may play an important role throughout the entire thickness of the

63   transition zone. Water solubility in majorite garnet synthesized at transition zone pressures and

64   temperatures can contain up to ~ 700 ppm wt H_2O (Bolfan-Casanova et al. 2000; Katayama et al.

65   2003), a quantity sufficient to radically change the deformation characteristics of garnet. For a

66   more complete understanding of the implications of OH defects in garnet in the deep mantle,

67   systematic computational studies of hydrogen incorporation into majorite are required.

68   At low pressures, H substitution in andradite garnet ($Ca_3Fe_2Si_3O_{12}$) takes place via the

69   hydrogarnet defect in which 4 hydrogen atoms charge balance a vacancy ordinarily occupied by

70   a Si atom in the tetrahedral site (Lager et al. 1989). However, the hydrogarnet defect is

71   associated with a volume expansion of the tetrahedral site (e.g., Lager et al. 1989; Purton et al.

72   1992) due to the change in Coulomb forces caused by the Si vacancy and also to accommodate

73   the hydrogen bonded network. This volume expansion should be less energetically favorable at

74   high pressure. Infrared absorption spectra indicate that OH is potentially incorporated into

75   majorite by formation of the hydrogarnet defect (Katayama et al. 2003).   However, water

76   concentrations in natural garnet samples brought to the surface from the mantle (Bell and

77   Rossmann 1992a, 1992b) and infrared spectroscopy of both natural garnet (Amthauer and

78   Rossman 1998; Beran and Libowitzky 2006) and synthetic majorite (Bolfan-Casanova et al.

79   2000) indicate that hydrogen incorporation in majorite may be complex (Williams and Hemley

80   2001). Therefore a systematic investigation of the hydrogen uptake mechanism in majorite is

81   necessary to clarify the situation.

82   Lateral variations in seismic body wave velocities throughout the mantle are caused by

83   temperature and compositional (i.e., water concentration, iron content, partial melting)

84   heterogeneities (Karato 2006). The hydration of transition zone minerals affects the seismic data

85   used to infer high- and low- temperature anomalies and interpretation of mantle plumes and

86   subducted slabs. The seismic ratio, $R=dlnV_s/dlnV_P$ can be used to differentiate between thermal

87   and compositional effects (Karato and Karki 2001). Indeed variations in seismic velocities,

88   expressed as $dlnV_s/dlnV_P$, have been used to suggest a strategy to disentangle the effects of

89   temperature and water content for ringwoodite and wadsleyite (Panero 2010; Li et al. 2011). The

90   temperature and pressure dependence of majorite sound velocities have been established

4

91 experimentally (Irifune et al. 2008; Sinogeiken and Bass 2002). Constraining the effect of water

92 on majorite elasticity is critical to the accurate interpretation of seismic velocities in Earth's

93 transition zone.

94   By analogy with other H defects in high-pressure silicates, H is likely incorporated into

95 the dodecahedral, octahedral, and tetrahedral sites of the majorite structure. While interstitial

96 hydrogen incorporation is possible in olivine (Balan et al. 2014), it is not likely in the denser

97 garnet structure at high-pressure. Thus, we present a computational investigation of the

98 energetics and associated geophysical properties (*P*- and *S*-waves velocities) resulting from

99 hydrogen incorporation in majorite via $[V_{Mg} + 2OH_O]^X$ and $[V_{Si} + 4OH_O]^X$ defects. By comparing

100 the defect energies associated with these different site substitutions of hydrogen, we determine

101 the most favorable hydrogen-defect mechanism. Additionally, we further investigate the

102 influence of aluminum on hydrogen incorporation and wave speeds.

103   **Computational methods**

104   The energies associated with hydrogen and aluminum incorporation in tetragonal

105 majorite garnet ($MgSiO_3$) were calculated as a function of pressure up to $P = 25$ GPa using

106 classical atomistic simulations based on the Born model of solids, as implemented in the General

107 Utility Lattice Program (GULP) (Gale and Rohl 2003).

108   The initial majorite structure was generated according to the experimental single-crystal

109 structure refinement (Angel et al. 1989). Mg and Si are assumed to be ordered over the 2

110 symmetrically unique octahedral sites based on the low concentration of aluminum (< ~8 wt%

111 Al_2O_3) and temperature ($T = 0$ K) (Nakatsuka et al. 1999; Vinograd et al. 2006). Majorite lattice

112 energy minimizations were performed using the full body-centered tetragonal unit cell, which

113 consists of 160 atoms.

114   Interatomic potential functions were used to describe the total lattice energy in terms of

115   the atomic positions. We adopt the fractional charges of Vinograd et al. (2006) where ionic

116   charges are scaled by 0.85 to improve transferability with respect to cation-cation distances. The

117   internal lattice energy is dominated by the Coulomb interactions and evaluated using an Ewald

118   summation. We modeled the short-range interactions between closed shell ionic species using a

119   Buckingham potential of the form;

120    $U_{sr} = \sum_{ij} A_{ij} exp\left(-\frac{r_{ij}}{\rho_{ij}}\right) - \frac{C_{ij}}{r_{ij}^6}$ (1)

121   where A, ρ, and C are empirically derived parameters. The sum is over pairs of ions, i and j ($i \neq$

122   j), with a separation distance, r_{ij}. Cutoffs for the Buckingham potentials are 10.0 Å for hydrogen

123   interactions and 12.0 Å for oxygen-oxygen and cation-oxygen interactions. These potentials are

124   tapered to zero over a range of 2.0 Å to ensure smoothness of the potential energy surface (Mei

125   et al. 1991).

126   Due to the partial covalence of the Si-O bond (Pauling 1980), a harmonic angle-bending

127   term was also included:

128    $U_{ijk} = \frac{1}{2} k_\theta (\theta - \theta_0)^2$ (2)

129   This was applied for both the Si-O and Al-O tetrahedra and octahedra in order to add an energy

130   penalty when there is a deviation from the coordination-dependent equilibrium bond angle.

131   Three-body terms applied to the majorite Si-O and Al-O polyhedra were defined based on

132   bonding between ions, which was defined to be fixed during relaxation, rather than cutoff

133   distances. The three-body contribution to the optimized total energy was confirmed to ensure

134   that the bonding was correctly defined for each system such that no spurious terms were present.

135   A shell model (Dick and Overhauser 1958) was adopted to account for the polarisability of the

136 oxygen anions. The O core-shell interactions are described by spring constants with the

137 functional form:

$$U = \frac{1}{2}k_2 r^2 + \frac{1}{24}k_4 r^4 \qquad (3)$$

139 The short-range bonded O-H interaction was described using a Coulomb-subtracted Morse

140 potential (Saul et al. 1985);

$$U_r = D_e\left[\left(1 - \exp\left(-a(r - r_0)\right)\right)^2\right] - \frac{q_i q_j}{r} \qquad (4)$$

142 where r_0 is the equilibrium bond length, q is the charge of the species, D_e and a are both fitted

143 parameters physically related to the molecular dissociation energy and vibrational frequency.

144 Here the Coulomb term is expressed in atomic units. The Morse potential is cutoff at 1.3 Å,

145 while the Buckingham potential is excluded for the intramolecular interaction within the

146 hydroxyl group.

147   Interatomic potential parameters (Table 1) developed for the anhydrous majorite-pyrope

148 solid solution (Vinograd et al. 2006) were augmented with force field parameters derived by

149 fitting to experimental structural and elastic properties of brucite, $Mg(OH)_2$, at both 0 GPa and

150 high pressure (Catti et al. 1995; Jiang et al. 2006). Due to the different fractional charge of the

151 hydroxyl oxygen ($O^{-1.2}$) compared to the non-hydroxyl oxygen ($O^{-1.7}$), we derived the

152 Buckingham potential parameter, *A*, by fitting to data for brucite. The two-body potentials for

153 the interaction between the hydroxyl oxygen and both Al and Si were generated from those for

154 the equivalent interaction for non-hydroxyl oxygen using scaling of coefficients (Schröder et al.

155 1992) by 0.709 assuming:

$$\frac{A_{Mg-O^{-1.2}}}{A_{Mg-O^{-1.4}}} = \frac{A_{Si-O^{-1.2}}}{A_{Si-O^{-1.4}}} = \frac{A_{Al-O^{-1.2}}}{A_{Al-O^{-1.4}}} \qquad (5)$$

157 Validation of the potential model was accomplished through calculation of the structural

158 relaxation, including unit-cell parameters, and elasticity of majorite for pressures between 0 and

159 25 GPa. Additionally, we calculate the structure and elasticity of superhydrous B,

160 $Mg_{10}Si_3O_{14}(OH_4)$, for pressures between 0 and 25 GPa and the zero-pressure structure and bulk

161 modulus of pyrope, corundum, α-quartz, coesite, stishovite, MgO, brucite, kaolinite, and lizardite

162 using the interatomic potentials in Table 1.

163 A Newton-Raphson optimizer, with Broyden-Fletcher-Goldfarb-Shanno (BFGS)

164 updating of the Hessian matrix, was used for energy minimization. When the gradient norm

165 reached 0.1, we switched to rational function optimization (RFO) to ensure that the final state

166 attained had positive definite curvature. The phonon density of states was also calculated to

167 verify the absence of imaginary modes within the Brillouin zone.
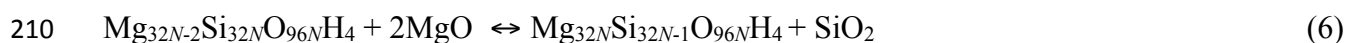
168 Energy minimizations were performed on the majorite structure with both charged and

169 charge-neutral point defects. Intrinsic vacancies were created by removal of a single atom or

170 bound Mg-O pairs where the Mg and O are nearest neighbors. Using the Kröger-Vink defect

171 notation, the intrinsic vacancy defects are expressed as V_{Mg}'', V_{Si}'''', and $V_O^{..}$. We calculated

172 Schottky defect energies in the form of vacancies where the negatively charged cation vacancy is

173 balanced by a positively charged oxygen vacancy. For mass balance, the atoms that are removed

174 are assumed to form a crystalline solid whose lattice energy also contributes to the Schottky

175 defect energy. The extrinsic defects $OH_O^.$, Al_{Si}', $Al_{Mg}^.$, $[V_{Mg} + 2OH_O]^X$, $[V_{Si} + 4OH_O]^X$, $[Al_{Si} +$

176 $Al_{Mg} + V_{Mg} + 2OH_O]^X$, and $[Al_{Si} + Al_{Mg} + V_{Si} + 4OH_O]^X$ were introduced by generating

177 vacancies and introducing impurities as appropriate. For the $OH_O^.$ defect, the H atom was

178 initially placed at three different positions relative to each oxygen site and energy minimization

179 calculations were run to determine the lowest energy configuration. The lowest energy

180 configuration was then used for the high-P calculations and we do not see a change in the

181   relaxed hydrogen configuration up to 25 GPa. The difference in energy between the defective

182   and the defect-free majorite lattice was taken to be the defect formation energy. Calculations

183   with a single $[V_{Mg} + 2OH_O]^X$ or $[V_{Si} + 4OH_O]^X$ defect complex per unit cell contain $0.56 - 1.1$

184   wt% H_2O and thus additional simulations were performed using 2 x 2 x 2 supercells (1280

185   atoms) for a more realistic concentration of hydrogen within the system (700 – 1400 ppm wt

186   H_2O) and to assess the influence of defect-defect interactions through the periodic boundary

187   conditions.   The initial atomic positions of impurities were determined visually using GDIS

188   (Fleming and Rohl 2005) and confirmed after optimization. The lattice parameters for the

189   pressure of interest were generated from constant pressure optimizations of the defect-free, bulk

190   cell.   Charged defect calculations are performed in the presence of a uniform neutralizing

191   background charge at constant volume. The initial fractional coordinates for the high-pressure

192   calculations involving charged defects were taken from the optimization at the previous lower

193   pressure. This ensures that a consistent configuration is being considered as a function of

194   pressure. Calculations involving majorite with charge-neutral defect complexes or any

195   calculation involving a defect-free phase were performed at constant pressure.
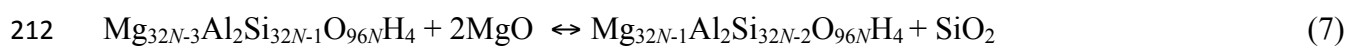
196   Complementary first-principles simulations were conducted at zero-pressure and $P = 20$

197   GPa for the most energetically favorable charge-balanced defect complexes as determined by the

198   atomistic simulations.   Static, DFT calculations were performed with VASP (Kresse and

199   Furthmüller 1996a, 1996b).   Ultrasoft pseudopotentials were used and calculations were

200   performed using the Perdew-Wang 1991 (PW91) formalism of the generalized gradient

201   approximation (GGA) for the exchange-correlation functional (Perdew 1991).   All first-

202   principles calculations were performed using a plane-wave cutoff of 600 eV with an energy

203   convergence criterion of 0.001 eV for optimization. The majorite calculations are performed at

204   the Γ point for Brillouin zone sampling due to the size of the unit cell. In contrast, the MgO and

205   SiO$_2$ calculations are averaged over Monkhorst-Pack grids of dimensions 16 x 16 x 16 and 8 x 8

206   x 8 k-points, respectively. To increase computational efficiency, all structures were first relaxed

207   at constant volume then subsequently relaxed at constant pressure.

208   The relative stability of the two defect mechanisms, $[V_{Mg} + 2OH_O]^X$ and $[V_{Si} + 4OH_O]^X$

209   was determined by calculating the enthalpy according to the reactions;

210    $Mg_{32N-2}Si_{32N}O_{96N}H_4 + 2MgO \leftrightarrow Mg_{32N}Si_{32N-1}O_{96N}H_4 + SiO_2$ (6)

211   and

212    $Mg_{32N-3}Al_2Si_{32N-1}O_{96N}H_4 + 2MgO \leftrightarrow Mg_{32N-1}Al_2Si_{32N-2}O_{96N}H_4 + SiO_2$ (7)

213   where N is the number of unit cells, with the assumption that the $[V_{Mg} + 2OH_O]^X$ defects are non-

214   interacting.   The   enthalpy   of   SiO$_2$ was   calculated   while   accounting   for   the   α-

215   quartz→coesite→stishovite phase transitions as a function of increasing pressure. The MgO and

216   SiO$_2$ calculations   were   performed   using   the   same   interatomic   potentials   (GULP)   and

217   pseudopotentials (VASP) as for the majorite calculations, and the initial unrelaxed structures

218   were taken from the American Mineralogist Crystal Structure Database (AMSCD) (Hazen 1976;

219   Levien and Prewitt 1981; Levien et al. 1980; Ross et al. 1990). This reaction does not involve

220   free H$_2$O due to the difficulty of modeling the energetics of supercritical water.

Results

Validation of calculations

223   The calculated majorite structure (Figure 1) (Supplemental data: Table S2) reproduces

224   the experimentally determined structure (Angel et al. 1989) as we find good quantitative

225   agreement between our calculated results and those previously determined from both theory and

226   experiment (Table 2). The structural parameters are within 0.6% of the experimental values,

227   while the errors are less than 6% for most elastic constants with the exception of C_{12} and C_{16}

228   (Table 3). Our calculated zero-pressure bulk modulus and shear modulus are within the spread

229   of experimental results and at $P = 10$ GPa deviate from experimental data (Sinogeikin and Bass

230   2002) by less than 3.5% (Table 3; Supplemental data: Figure S1). Results from our static lattice-

231   energy calculations (SLEC) and the results from Vinograd et al. (2006) were obtained using

232   essentially the same potential models, except for changes to the truncation of the Buckingham

233   potentials and the inclusion of a fourth-order spring constant in the shell model. Hence, the

234   agreement here is to be expected. For phases other than majorite, we find agreement between our

235   calculations and experimentally determined values (Supplemental data: Table S3, Figure S2),

236   with differences of less than ~5% for all structural parameters and ~13% for most bulk moduli.

237   The greatest differences in bulk moduli are for MgO and brucite due to the inability of a simple

238   shell-model to capture the well-known Cauchy violation ($C_{12} \neq C_{14}$) in periclase (Catlow et al.

239   1976) and the limited transferability of the interatomic potentials to non-silicates. Our first-

240   principles calculations reproduce the experimental structure and are consistent with previous

241   DFT-GGA results (Table 2) (Supplemental data: Table S2).   The generalized gradient

242   approximation used here tends to lead to a systematic overestimation of structural parameters

243   when compared to experiment, consistent with the observations in the present study. The axial

244   ratio calculated at $P = 20$ GPa using DFT results is only 0.3% smaller than the force field

245   approach.

Defect energies in the absence of water incorporation

247   The enthalpy of charged Mg, Si, and O, vacancy formation in MgSiO$_3$ garnet were

248   calculated up to $P = 25$ GPa. The ^{VIII}Mg2 and ^{IV}Si2 sites are found to have the lowest energetic

249   cost for forming Mg and Si vacancies (Table 4; Supplemental data: Figure S3). The octahedral

250 site is significantly less favorable for both Mg and Si vacancy defects. The Schottky defect with

251 the lowest energy (E_{Schottky} = 4.48 – 7.24 eV) is the $[V_{\text{Mg2}} + V_{\text{O5}}]^X$ defect (Table 4) in which the

252 Mg-vacancy and O-vacancy are nearest neighbors with an additional energy cost of 0.07 – 0.26

253 eV when Mg2 and O5 vacancies are not nearest neighbors. Formation of a vacancy at the Mg1

254 site, which is bonded to all 6 oxygens, has a greater Schottky defect energy at zero-pressure

255 when the vacancies at the O1 and O2 sites are not nearest neighbors. Conversely at high

256 pressure, lower Schottky defect energies tend to be associated with Mg and O vacancies that are

257 nearest neighbors with the exception of V_{Mg1}'' neighboring $V_{\text{O1}}^{\cdot\cdot}$ or $V_{\text{O6}}^{\cdot\cdot}$. When considering the

258 silicon sites, $^{\text{IV}}$Si2 vacancies have the lowest Schottky defect energies (Table 4).

Protonation mechanism

260   Protonation of the O1, O4, and O5 sites have energies 0.3 - 0.6 eV lower than O2, O3,

261 and O6 at zero pressure (Figure 2). The protonation energetics can be explained by whether Si

262 (higher energy) or Mg (lower energy) occupies the octahedral site to which the protonated

263 oxygen is bonded. Among the octahedral-Mg oxygen sites, the O5 site is the most favorable site

264 for protonation with a defect formation energy 0.09-0.1 eV lower than O4 and O1. Protonation

265 of the O6 site is 0.20-0.21 eV less favorable compared to the other 2 sites (O2 and O3) involved

266 in Si octahedra.

267   At all pressures, the O5 site is the most likely to bind a hydrogen atom and the O5

268 protonation enthalpy increases with pressure at a smaller rate than for the other oxygen sites

269 (Figure 2). Furthermore, protonation of the oxygen sites involved in Si octahedra become less

270 favorable with pressure relative to the sites involved in Mg octahedra.

271   Based on the energetics associated with creating charged cation and oxygen vacancies,

272 neutral Schottky defects, and protonating the oxygen sites, we propose four distinct charge-

273   balanced hydrogen incorporation mechanisms in majorite. These mechanisms are $[V_{Mg2} +$

274   $2OH_{O5}]^X$, $[V_{Mg3} + 2OH_{O5}]^X$, $[V_{Si2} + 4OH_{O6}]^X$, and $[V_{Si4} + 2OH_{O2} + 2OH_{O3}]^X$. The proposed

275   mechanisms include the tetrahedral, octahedral, and dodecahedral sites. The defect structures, as

276   optimized at zero-pressure using the force field approach, are shown in Figure 3. We consider

277   hydrogen incorporation into the dodecahedral site as $[V_{Mg2} + 2OH_{O5}]^X$, into the octahedral sites

278   as either $[V_{Mg3} + 2OH_{O5}]^X$ or $[V_{Si4} + 2OH_{O2} + 2OH_{O3}]^X$, and into the tetrahedral site as the

279   hydrogarnet-type defect $[V_{Si2} + 4OH_{O6}]^X$. The optimized hydrogarnet defect consists of the 4 H

280   atoms lying outside of the Si-vacant tetrahedra along the edges and this configuration is

281   confirmed by the DFT calculations. The other three optimized defects show the H atoms

282   pointing inward toward the vacancy and region of negative charge. The DFT calculations also

283   result in the H atoms pointing inward for the $[V_{Mg3} + 2OH_{O5}]^X$ defect. However, there is a

284   difference in direction that the H atoms point. The force field calculations yield a configuration

285   in which the H atoms lie in the plane formed by the O4 and O5 atoms with the H atoms pointing

286   toward opposite O4 atoms ($\angle$O5-H-O1 = ~110°). The DFT optimization results in the H atoms

287   pointing toward opposite O1 atoms ($\angle$O5-H-O1 = ~160°).

288   The $[V_{Mg3} + 2OH_{O5}]^X$ octahedral-based defect has formation energy 0.07 eV less than the

289   dodecahedral-based $[V_{Mg2} + 2OH_{O5}]^X$ defect at zero-pressure (Supplemental data: Figure S4).

290   The formation enthalpy difference between the two different Mg defects decreases to 0.01 eV at

291   $P = 25$ GPa. Thus, our interpretation is that H-substitution balanced by Mg vacancies is as likely

292   to occur at octahedral sites as it is to occur at dodecahedral sites. At $P = 0$ GPa, the hydrogarnet

293   defect $[V_{Si2} + 4OH_{O6}]^X$ is 3.56 eV more favorable than hydrogen incorporation into the

294   octahedral site that is normally occupied by silicon (Supplemental data: Figure S4). The

295   enthalpy difference between the Si-based hydrogen defects increases with increasing pressure to
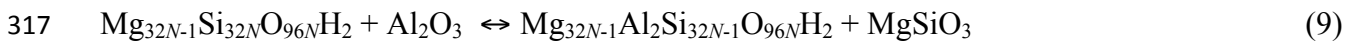
13

296   3.96 eV at 25 GPa, and therefore the octahedral defect is not expected at any relevant pressure.

297   The enthalpy for reaction 6, which is used to compare the relative stability of the hydrogarnet

298   defect with the $[V_{Mg3} + 2OH_{O5}]^{X}$ defect, is negative at all pressures (Figure 4) indicating that the

299   hydrogarnet defect should be significantly more stable in majorite at mantle pressures. The

300   stability of the hydrogarnet defect is verified by the DFT calculations (Table 5). The partitioning

301   of hydrogen between the Mg3 sites and Si2 sites can be calculated from the equilibrium constant,

302   K, of reaction 6 as;

303    $$D^{Si2/Mg3} = K = \exp\frac{-\Delta G}{RT} \sim \exp\frac{-\Delta H}{RT} \qquad\qquad (8)$$
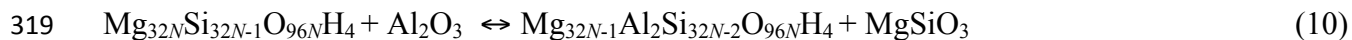
304   Because of a greater number of configurations with the Mg site over the Si site, entropic effects

305   will increase ΔG at high temperatures. Therefore, as an upper bound, the partition coefficient at

306   20 GPa and 1800 K is $D^{Si2/Mg3} \approx 200$.

307   **Effect of Al on OH incorporation**

308   Al is most likely to be incorporated into the majorite structure at either the Si2 tetrahedral

309   or the octahedral sites: the $Al_{Si4}{}'$ defect has a formation enthalpy that is only 0.13 eV less than

310   that of the $Al_{Si2}{}'$ defect at zero-pressure and their enthalpies are equal to each other at 25 GPa.

311   The $Al_{Mg3}{}^{\cdot}$ defect has a formation enthalpy that is at least 1.1 eV less than the enthalpy

312   associated with Al substitution for dodecahedral Mg over the entire pressure range. Therefore,

313   we propose that Al is incorporated into majorite via a coupled substitution with octahedral Mg

314   and either octahedral Si4 or tetrahedral Si2. We calculate the formation enthalpy of the $[V_{Mg3} +$

315    $2OH_{O5}]^{X}$ defect and the $[V_{Si2} + 4OH_{O6}]^{X}$ hydrogarnet defect in the presence of a coupled Al-

316   substitution either as $[Al_{Mg3} + Al_{Si2}]^{X}$ or $[Al_{Mg3} + Al_{Si4}]^{X}$. Based on the mass-balanced reactions;

317    $Mg_{32N-1}Si_{32N}O_{96N}H_2 + Al_2O_3 \leftrightarrow Mg_{32N-1}Al_2Si_{32N-1}O_{96N}H_2 + MgSiO_3 \qquad\qquad (9)$

318   and

319 $$Mg_{32N}Si_{32N-1}O_{96N}H_4 + Al_2O_3 \leftrightarrow Mg_{32N-1}Al_2Si_{32N-2}O_{96N}H_4 + MgSiO_3 \tag{10}$$

320 where Al_2O_3 is corundum and $MgSiO_3$ is majorite, both the $[V_{Mg3} + 2OH_{O5}]^X$ and the $[V_{Si2} +$

321 $4OH_{O6}]^X$ are more stable in the presence of a coupled Al-substitution at all pressures (Figure 5).

322 Additionally, according to reaction 7 (Figure 4), the presence of Al serves to further stabilize the

323 hydrogarnet defect relative to the $[V_{Mg3} + 2OH_{O5}]^X$. The reaction enthalpy as a function of

324 pressure for reactions 6 and 7 goes through a maximum due to the coesite-stishovite phase

325 transition in SiO_2. The maximum in reaction 6 occurs at 10-15 GPa but in reaction 7 it occurs at

326 7.5-10 GPa. We interpret this as the hydrogarnet defect being more energetically favorable at

327 lower pressures in the presence of Al.

328 **Influence of defect-defect interactions**

329 Comparison of the defect energies associated with both the single unit cell and 2 x 2 x 2

330 supercell of Al-free majorite shows that interaction of periodic images of the hydrogen defects is

331 insignificant ($\Delta H_{def} \leq 0.03$ eV) (Supplemental data: Figure S4). The defect-defect interactions

332 in aluminous majorite are more significant with the supercell calculations (0.4 wt% Al_2O_3)

333 resulting in hydrous defect formation enthalpies that are up to 0.39 eV greater than the

334 calculations using a single unit-cell (3.2 wt% Al_2O_3).

335 **Wave speeds in hydrous majorite**

336 To examine quantities that could provide geophysical evidence of hydrogen incorporation

337 in garnet in the upper mantle and transition zone, the Voigt-Reuss-Hill averages of the bulk and

338 shear moduli were calculated from the elastic constants (Anderson 1963) derived from the force

339 field calculations (Table 3) along with the compressional and shear acoustic velocities, V_p and V_s.

340 There is a negligible effect of water on both V_p and V_s for majorite with 700 – 1400 ppm wt H_2O

341 at 25 GPa (Figure 6). At these concentrations, body wave speeds are reduced by only ~0.2%,

342 unlikely to be detectable by seismological measurements within the limits of radial seismic

343 profile uncertainties (Matas et al. 2007). When normalized to the same water concentration

344 (1400 ppm wt H_2O) over the pressure range of this study, the shear modulus of majorite with the

345 $[V_{Si2} + 4OH_{O6}]^X$ defect is 0.3% greater than with the $[V_{Mg3} + 2OH_{O5}]^X$ defect. There is even less

346 of a difference between the bulk moduli (<0.2%) and no difference between the densities as a

347 function of defect mechanism. Significant effects on body-wave speeds can only be seen at

348 concentrations of >0.5 wt% water with reductions in V_p and V_s of 1-2% at transition zone

349 pressures. However, such concentrations of water in majoritic garnets are unlikely in Earth's

350 mantle (Beran and Libowitzky 2006)

351   **Discussion**

352 **Defect Mechanisms**

353   Bolfan-Casanova et al. (2000) synthesized tetragonal $MgSiO_3$ majorite at 17.5 GPa and

354 ~1800 K with ~680 ppm wt H_2O. They argue against the hydrogarnet substitution based on the

355 IR spectra citing the volume expansion of the Si-O tetrahedra (Lager et al. 1989) and energetic

356 feasibility of the hydrogarnet defect formation only at large water contents (Rossman and Aines

357 1991). The OH-absorption band in synthetic majorite (Bolfan-Casanova et al. 2000) is centered

358 80 cm^{-1} lower and is 65 cm^{-1} broader compared to the hydrogarnet OH-absorption band in

359 pyrope synthesized at high-pressure (Withers et al. 1998). The volume expansion of the

360 tetrahedra in andradite garnets (Lager et al. 1989) has been used to explain the apparent abrupt

361 dewatering of pyrope at high-pressure (Withers et al. 1998). However, a more recent study

362 (Mookherjee and Karato 2010) shows that pyrope does not dewater abruptly at $P = $ ~7 GPa.

363 Natural grossular garnets with low-OH contents have complex IR spectra and are thus proposed

364 to have substitution of H at the dodecahedral and octahedral site but no evidence for these

365 substitutions was presented (Rossman and Aines 1991). Our results show that even at low-water

366 contents, the hydrogarnet defect is likely to form in majorite. Synthesis of majorite in the

367 MORB + H_2O system results in a sharp peak centered at 3580 cm^{-1} (Katayama et al. 2003) which
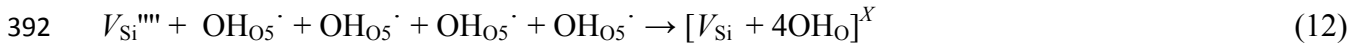
368 is only 20 cm^{-1} lower than the hydrogarnet substitution in synthetic pyrope (Ackermann et al.

369 1983). For the hydrogarnet defect in majorite (P = 0 GPa), our calculated bond lengths using

370 force field methods, d(O-O) = 2.83 and 3.24 Å for the shared and unshared edges, are shorter

371 than those in grossular (d(O-O) = 3.08 and 3.29 Å) also calculated using interatomic potentials

372 (Wright et al. 1994). Thus, the incorporation of hydrogen through the hydrogarnet defect causes

373 a greater tetrahedral volume expansion in grossular than in majorite due to a greater lengthening

374 of the 2 shared tetrahedral edges. This greater lengthening of the shared edges in grossular is

375 energetically favorable due to Ca, with its larger ionic radius, occupying the dodecahedral sites.

376 Additionally, our DFT optimizations of the hydrogarnet defect result in d(H…O) = 2.26-2.34 Å,

377 which is shorter than d(H…O) = 2.49-2.62 Å and d(H…O) = ~2.23-2.54 Å for katoite and

378 hydropyrope calculated in a previous first principles study (Nobes et al. 2000). The shorter

379 d(H…O) in majorite relative to hydropyrope is related to the O-H…O angle. The longer

380 calculated distances in hydroyrope are associated with O-H…O = 113-120° compared to 146-

381 147° in our majorite calculations. Based on shorter O…O and H…O distances, we expect the

382 OH-stretching vibrational frequency to be lower in majorite when compared to other garnets

383 (Libowitzky 1999). Thus it appears that the variation in the vibrational peak positions for the

384 hydrogarnet defect in garnet can be attributed to differences in major and trace element

385 chemistry and possibly the presence of an additional substitution mechanism.

386   Our calculated defect binding energies show that isolated hydroxyl groups are unlikely in

387 the majorite structure and hydrogen is associated with cation vacancies. The defect binding

388   energies for protonation of the ^{VI}Mg site and the formation of the hydrogarnet defect are

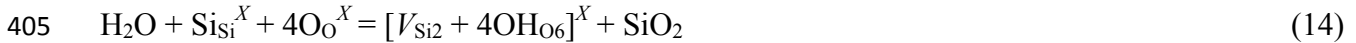389   calculated according to the reactions;

390     $V_{\mathrm{Mg3}}'' + \mathrm{OH_{O5}}^{\cdot} + \mathrm{OH_{O5}}^{\cdot} \rightarrow [V_{\mathrm{Mg3}} + 2\mathrm{OH_{O5}}]^{X}$ (11)

391   and

392     $V_{\mathrm{Si}}'''' + \mathrm{OH_{O5}}^{\cdot} + \mathrm{OH_{O5}}^{\cdot} + \mathrm{OH_{O5}}^{\cdot} + \mathrm{OH_{O5}}^{\cdot} \rightarrow [V_{\mathrm{Si}} + 4\mathrm{OH_O}]^{X}$ (12)
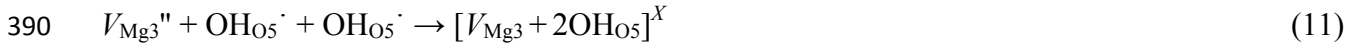
393   The energetics for formation of the hydrogarnet and $[V_{\mathrm{Mg3}} + 2\mathrm{OH_{O5}}]^{X}$ defects are thus -2.19 eV/H

394   and -1.09 eV/H at zero-pressure. The binding energies become more exothermic with increasing

395   pressure to -2.87 eV/H and -1.64 eV/H at 25 GPa confirming that isolated defects become less

396   favorable at high pressure. The preferential formation of the hydrogarnet defect is consistent

397   with atomistic simulations of hydrogen defect formation in ringwoodite (Blanchard et al. 2005).

398   However, Blanchard et al. (2005) show a significantly greater driving force for hydrogen to be

399   bound to cation vacancies in ringwoodite with defect binding energies of -15.80 eV/H and -10.36

400   eV/H. This is consistent with the greater H_2O storage capacity of ringwoodite (e.g., Bolfan-

401   Casanova 2005).

402   We also compare the relative defect energies of the two defect mechanisms through the

403   reaction of majorite with water as:

404     $H_2O + \mathrm{Mg_{Mg}}^{X} + 2\mathrm{O_O}^{X} = [V_{\mathrm{Mg3}} + 2\mathrm{OH_{O5}}]^{X} + \mathrm{MgO}$ (13)

405     $H_2O + \mathrm{Si_{Si}}^{X} + 4\mathrm{O_O}^{X} = [V_{\mathrm{Si2}} + 4\mathrm{OH_{O6}}]^{X} + \mathrm{SiO_2}$ (14)

406   The reaction energies are thus calculated according to;

407     $E_{12} = E_{\mathrm{Mg\text{-}OH}} + E_{\mathrm{PT}} + U_{\mathrm{MgO}}$ (15)

408     $E_{13} = E_{\mathrm{Hydrogarnet}} + 2E_{\mathrm{PT}} + U_{\mathrm{SiO_2}}$ (16)

409   where E_{PT} is the proton transfer energy and assumed to be -9.74 eV at zero-pressure. The

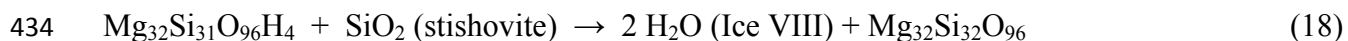410   derivation of E_{PT} and the full Born-Haber thermochemical cycle for hydrolysis reactions can be

found elsewhere (Catlow 1977; Wright et al. 1994). Our zero-pressure calculations show that the hydrogarnet defect is more favorable by 1.44 eV with large negative energies of -6.51 eV/H and -7.95 eV/H for reactions 12 and 13. Thus, it is possible that both types of defects occur in majorite with the hydrogarnet defect likely to be dominant. This is consistent with IR spectra that show a deviation from a strict hydrogarnet substitution (Bolfan-Casanova et al. 2000). Atomistic simulations of defect mechanisms in the olivine polymorphs also show that one defect mechanism tends to be favored over the other. In the case of ringwoodite, both mechanisms are energetically favorable with reaction energies of -3.08 eV/H and -6.49 eV/H (Blanchard et al. 2005) and as with majorite, the hydrogarnet is more likely to be dominant. The hydrogarnet defect is also likely to occur in olivine with a reaction energy of 0.4 eV/H compared to 1.5 eV/H for the $[V_{Mg} + 2OH_O]^X$ defect (Walker et al. 2006). Conversely, the $[V_{Mg} + 2OH_O]^X$ is 5 eV more favorable than the hydrogarnet defect in wadsleyite (Walker et al. 2006).

Comparison of our DFT-GGA results at 20 GPa (Table 5) with the work of Panero (2010) confirms that the hydrogarnet defect is more likely to occur in majorite than in ringwoodite. The $[V_{Mg} + 2OH_O]^X$ defect is 0.54 eV/H more favorable in ringwoodite than in majorite, while the hydrogarnet defect formation enthalpy in majorite is 0.12 eV/H less than in ringwoodite. Reaction 3 shows that the hydrogarnet defect is more stable in ringwoodite by 0.17 eV/H (Panero 2010) compared to 0.82 eV/H in majorite.

The stability of the hydrous defects relative to the anhydrous phase in the presence of free H_2O at high-pressure can be accomplished through static calculations using Ice VIII (Panero 2006). The following reactions at 20 GPa are considered;

$$Mg_{31}Si_{32}O_{96}H_2 + MgO \rightarrow H_2O \text{ (Ice VIII)} + Mg_{32}Si_{32}O_{96} \qquad (17)$$

and

434      $Mg_{32}Si_{31}O_{96}H_4 + SiO_2$ (stishovite) $\rightarrow$ 2 H_2O (Ice VIII) + $Mg_{32}Si_{32}O_{96}$ (18)
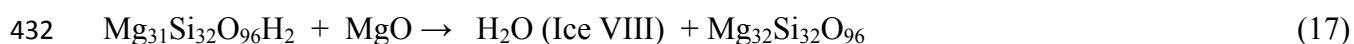
435   resulting in calculated static reaction enthalpies of -1.88 eV and -0.47 eV respectively.

436   Considering the heat of fusion of H_2O at ambient conditions (0.06 eV) and assuming the Dulong-

437   Petit limit, the relative enthalpy of reaction 17 increases to 0.09 eV at 20 GPa and 2000 K.

438   However, this represents an upper bound because the entropic effects of supercritical water are

439   not considered here. Thus it appears more likely that the hydrogarnet defect will be stable at

440   transition zone conditions and the $[V_{Mg} + 2OH_O]^X$ defect may not occur at high P-T in the

441   presence of water. This supports the interpretation that it is solely the hydrogarnet defect found

442   in the IR spectra of Katayama et al. (2003).

443   It is possible that there are other H-defect mechanisms in majorite besides those

444   considered here. Zhang and Wright (2010) show that coupled substitutions of Al and H into

445   forsterite favors hydrogen substitution at the Si site by 1-2 eV/H. Our calculations show that the

446   presence of Al stabilizes the hydrogarnet defect by 2.2-2.4 eV (Figure 4). However, Mookherjee

447   and Karato (2010) propose that water is incorporated into pyrope at high water contents through

448   the $[(Al+H)_{Si}]^X$ defect.

449   Majoritic garnet found in diamond inclusions originating from transition zone depths

450   have been found to contain ~1 wt% Na_2O coupled with ~15-20 wt% Al_2O_3 (Stachl 2001).

451   However, these garnet inclusions are most likely anhydrous with the weight percent of major and

452   minor element oxides summing to >100%. Zhang and Wright (2012) show that the presence of

453   Al^{3+} and the monovalent Li ion may increase the potential of olivine to incorporate water, with

454   the hydrogarnet defect being particularly favorable. Therefore it may be possible that coupled

455   substitution of Na^+ and Al^{3+} promotes hydrogen uptake in garnet as well.

456   The presence of iron in majorite may also affect the type of defect mechanism present in

457   majorite. Atomistic simulations show that in reducing environments, it is favorable for water to

458   be incorporated at vacant oxygen sites formed through reduction of ferric iron to ferrous iron

459   (Wright and Catlow 1994). Indeed, incorporation of water in olivine through Fe redox exchange

460   has been observed experimentally (Demouchy and Mackwell 2006). However, IR-spectra of Fe-

461   bearing ringwoodite collected at high-pressure (>20 GPa) and low-temperature (5 K) show that

462   water is incorporated at both the octahedral site and through the hydrogarnet defect with

463   multiple defect mechanisms leading to the broad OH-absorption band observed in ringwoodite at

464   higher temperatures (Panero et al. 2013). Therefore, we predict that the hydrogarnet defect is the

465   most stable and dominant defect mechanism in majorite, with the presence of multiple defect

466   mechanisms likely.

467   **Implications**

468   The partitioning of water between mineral phases of the transition zone is dependent

469   upon the type of defect mechanism present in each phase (Keppler and Bolfan-Casanova 2006).

470   If both ringwoodite and majorite incorporate water mainly through the hydrogarnet substitution,

471   partitioning between the two phases is independent of water fugacity. Considering that ~1.4

472   wt% H_2O has been observed in a natural ringwoodite inclusion in a diamond from the transition

473   zone (Pearson et al. 2014), this suggests that majorite in the transition zone may contain 700 ppm

474   water, at least locally in the CH_4-rich environments that are conducive to diamond formation.

475   Majorite with water concentrations this large have been shown to be stable in synthesis

476   experiments at lower transition zone pressure-temperature conditions (Bolfan-Casanova et al.

477   2000; Katayama et al. 2003).

478   Lateral heterogeneities in seismic wave speeds in the Earth's upper mantle can be caused

479   by both variations in composition and temperature. The $R(H_2O)$ ratio of $d\ln(Vs)/d(H_2O)$ and

480    $d\ln(Vp)/d(H_2O)$ and the $R(T)$ ratio of $d\ln(Vs)/dT$ and $d\ln(Vp)/dT$ are useful to elucidate the

481   underlying cause of mantle heterogeneities (Li et al. 2011). We calculate $R(H_2O)$ for Al-free

482   majorite as;

483    $R(\mathrm{H_2O}) = \dfrac{\ln V_S(1400 \text{ ppm wt } \mathrm{H_2O}) - \ln V_S(\text{anhydrous})}{\ln V_p(1400 \text{ ppm wt } \mathrm{H_2O}) - \ln V_p(\text{anhydrous})}$ (19)

484   The $R(T)$ value for majorite was calculated at 16 GPa such that;

485    $R(\mathrm{T}) = \dfrac{\ln V_S(1473 \text{ K}) - \ln V_S(300 \text{ K})}{\ln V_p(1473 \text{ K}) - \ln V_p(300 \text{ K})}$ (20)

486   based on the ultrasonic measurements of Irifune et al. (2008). $R(H_2O)$ for ringwoodite was taken

487   from Panero (2010) and Li et al. (2011). The Li et al. (2011) seismic ratios for olivine,

488   wadslyeite, and ringwoodite were determined using experimental and calculated densities, bulk

489   and shear moduli (Inoue et al. 1998; Li et al. 2009; Liu et al. 2009; Mao et al. 2008, 2010;

490   Tsuchiya and Tsuchiya 2009; Wang et al. 2003). Even though water at the ~1000 ppm level has

491   only a minor effect on the absolute body wave speeds (Figure 6), our calculated $R(H_2O)$ values

492   show that the presence of hydrated majorite is observable (Figure 7) within the typical seismic

493   model uncertainty of ± 0.15 (Karato and Karki 2001). The presence of Al has a significant effect

494   on $R(H_2O)$, with our calculations showing that R decreases by ~0.2-0.4 in the presence of 3 wt%

495   Al_2O_3 with the Al substituted into the octahedral sites. Additionally, seismic wave speeds are

496   dependent upon the density, bulk modulus, and shear modulus thus the pressure dependence of R

497   is particularly sensitive to the pressure derivatives of these parameters. In addition to pressure

498   and temperature, compositional variations, such as variations in Fe content can strongly

499   influence seismic ratios. However, even when considering the presence of Al, $R(H_2O)$ for

500   majorite appears to be significantly different than the same ratio for ringwoodite at high

501 pressures with a difference of 0.5-1.2 at 20 GPa. At the base of the transition zone, $R(H_2O)$ for

502 majorite is indistinguishable from $R(T)$ of ringwoodite calculated by Li et al. (2011) using DFT.

503 $R(T)$ for majorite is ~0.5-1.0 greater than our calculated $R(H_2O)$ for majorite. Our calculated

504 $R(H_2O)$ for Al-free majorite is indistinguishable from that of olivine and wadsleyite up to 15 and

505 20 GPa but becomes significantly different in the presence of aluminum. Therefore, it appears

506 that the effect of hydrated, aluminous majorite should be visible in the upper mantle and

507 neglecting it may result in an overestimate of temperature anomalies.

520 **References Cited**

521 Ackermann, L., Cemic, L. and Langer, K. (1983) Hydrogarnet substitution in pyrope - a

522   possible location for "water" in the mantle. Earth and Planetary Science Letters, 62, 208-

523   214.

524   Amthauer, G. and Rossman, G.R. (1998) The hydrous component in andradite garnet. American

525   Mineralogist, 83, 835-840.

526   Anderson, O.L. (1963) A simplified method for calculating Debye temperature from elastic

527   constants. Journal of Physics and Chemistry of Solids, 24, 909-917.

528   Andrault, D., Angel, R.J., Mosenfelder, J.L., and Le Bihan, T. (2003) Equation of state of

529   stishovite to lower mantle pressures, American Mineralogist, 88, 301-307.

530   Angel, R.J., Finger, L.W., Hazen, R.M., Kanzaki, M., Weidner, D.J., Liebermann, R.C. and

531   Veblen, D.R. (1989) Structure and twinning of single-crystal $MgSiO_3$ garnet synthesized

532   at 17 GPa and 1800 °C. American Mineralogist, 74, 509-512.

533   Angel. R.J., Allan, D.R., Miletich, R., and Finger, L.W. (1997) The use of quartz as an internal

534   pressure standard in high-pressure crystallography. Journal of Applied Crytallography,

535   30, 461-466.

536   Angel, R.J., Mosenfelder, J.L., and Shaw, C.S.J. (2001) Anomalous compression and equation of

537   state of coesite. Physics of the Earth and Planetary Interiors, 124, 71-79.

538   Balan, E., Blanchard, M., Lazzeri, M., and Ingrin, J. (2014) Contribution of interstitial OH

539   groups to the incorporation of water in forsterite. Physics and Chemistry of Minerals, 41,

540   105-114.

541   Bass, J.D., Liebermann, R.C., Weidner, D.J., and Finch, S.J. (1981) Elastic properties from

542   acoustic and volume compression experiments. Physics of the Earth and Planetary

543   Interiors, 25, 140-158.

544   Bell, D.R. and Rossman, G.R. (1992) Water in Earth's mantle - the role of nominally

545   anhydrous minerals. Science, 251, 1391-1397.

546   Bell, D.R. and Rossman, G.R. (1992) The distribution of hydroxyl in garnets from the

547   subcontinental mantle of southern Africa. Contributions to Mineralogy and Petrology,

548   111, 161-178.

549 Beran, A. and Libowitzky, E. (2006) Water in natural mantle minerals II: Olivine, garnet and

550   accessory minerals. In H. Keppler and J.R. Smyth, Eds., Water in Nominally Anhydrous

551   Minerals, 62, p. 169-191, Reviews in Mineralogy and Geochemistry, Mineralogical

552   Society of America, Chantilly, Virginia.

553 Bish, D.L. (1993) Rietveld refinement of the kaolinite structure at 1.5 K. Clays and Clay

554   Minerals, 41, 738-744.

555 Blanchard, M., Wright, K. and Gale, J.D. (2005) A computer simulation study of OH defects in

556   Mg_2SiO_4 and Mg_2GeO_4 spinels. Physics and Chemistry of Minerals, 32, 585-593.

557 Bolfan-Casanova, N. (2005) Water in the Earth's mantle. Mineralogical Magazine, 69, 229-257.

558 Bolfan-Casanova, N., Keppler, H. and Rubie, D.C. (2000) Water partitioning between nominally

559   anhydrous minerals in the MgO-SiO_2-H_2O system up to 24 GPa: implications for the

560   distribution of water in the Earth's mantle. Earth and Planetary Science Letters, 182, 209-

561   221.

562 Catlow, C.R.A. (1977) Oxygen incorporation in alkaline-Earth fluorides. Journal of Physics and

563   Chemistry of Solids, 38, 1131-1136.

564 Catlow, C.R.A., Faux, I.D. and Norgett, M.J. (1976) Shell and breathing shell model

565   calculations for defect formation energies and volumes in magnesium oxide. Journal of

566   Physics C-Solid State Physics, 9, 419-429.

567 Catti, M., Ferris, G., Hull, S., and Pavese, A. (1995) Static compression and H disorder in

568   brucite, $Mg(OH)_2$, to 11 GPa: a powder neutron diffraction study. Physics and Chemistry

569   of Minerals, 22, 200-206.

570   Demouchy, S. and Mackwell, S. (2006) Mechanisms of hydrogen incorporation and diffusion in

571   iron-bearing olivine. Physics and Chemistry of Minerals, 294, 347-355.

572   Dick, B.G. Jr. and Overhauser, A.W. (1958) Theory of the dielectric constants of alkali halide

573   crystals. Physical Review, 112, 90-103.

574   Finger, L.W. and Hazen, R.M. (1978) Crystal structure and compression of ruby to 46 kbar.

575   Journal of Applied Physics, 49, 5823.

576   Fleming, S. and Rohl, A. (2005) GDIS: a visualization program for molecular and periodic

577   systems. Zeitschrift für Kristallographie, 220, 580–584.

578   Frost, D.J. (2008) The upper mantle and transition zone. Elements, 4, 171-176.

579   Gale, J.D. and Rohl, A.L. (2003) The general utility lattice program (GULP). Molecular

580   Simulation, 29, 291-341.

581   Gwamnesia, G.D., Chen, G., and Liebermann, R.C. (1998) Sound velocities in $MgSiO_3$-garnet to

582   8 GPa. Geophysical Research Letters, 25, 4553-4556.

583   Hazen, R.M. (1976) Effects of temperature and pressure on cell dimension and x-ray

584   temperature factors of periclase. American Mineralogist, 61, 266-271.

585   Hirschmann, M.M. (2006) Water, melting, and the deep Earth H_2O cycle. Annual Review of

586   Earth and Planetary Sciences, 34, 629-653.

587   Inoue, T., Weidner, D.J., Northrup, P.A. and Parise, J.B. (1998) Elastic properties of hydrous

588   ringwoodite (gamma-phase) in Mg_2SiO_4. Earth and Planetary Science Letters, 160, 107-

589   113

590   Irifune, T., Higo, Y., Inoue, T., Kono, Y., Ohfuji, H. and Funakoshi, K. (2008) Sound velocities

591   of majorite garnet and the composition of the mantle transition region. Nature, 451, 814-

592   817.

593   Jacobsen, S.D., Reichmann, H.-J., Spetzler, H.A., Mackwell, S.J., Smyth, J.R., Angel, R.J., and

594   McCammon, C.A. (2002) Structure and elasticity of single-crystal (Mg,Fe)O and a new

595   method of generating shear waves for gigahertz ultrasonic interferometry. Journal of

596   Geophysical Research, 107, 2037.

597   Jiang, F., Speziale, S., and Duffy, T.S. (2006) Single-crystal elasticity of brucite, $Mg(OH)_2$, to 15

598   GPa by Brillouin scattering. American Mineralogist, 91, 1893-1900.

599   Karato, S. (2006) Remote sensing of hydrogen in Earth's mantle. In H. Keppler and J.R. Smyth,

600   Eds., Water in Nominally Anhydrous Minerals, 62, p. 343-375, Reviews in Mineralogy

601   and Geochemistry, Mineralogical Society of America, Chantilly, Virginia.

602   Karato, S. and Karki, B.B. (2001) Origin of lateral variation of seismic wave velocities and

603   density in the deep mantle. Journal of Geophysical Research, 106, 21771-21783.

604   Katayama, I., Hirose, K., Yurimoto, H. and Nakashima, S. (2003) Water solubility in majoritic

605   garnet in subducting oceanic crust. Geophysical Research Letters, 30, 2155.

606   Keppler, H. and Bolfan-Casanova, N. (2006) Thermodynamics of water solubility and

607   partitioning. In H. Keppler and J.R. Smyth, Eds., Water in Nominally Anhydrous

608   Minerals, 62, p. 193-230, Reviews in Mineralogy and Geochemistry, Mineralogical

609   Society of America, Chantilly, Virginia.

610   Kohlstedt, D.L., Keppler, H. and Rubie, D.C. (1996) Solubility of water in the alpha, beta and

611   gamma phases of $(Mg,Fe)_2SiO_4$. Contributions to Mineralogy and Petrology, 123, 345-

612   357.

613   Kresse, G. and Furthmüller, J. (1996) Efficiency of ab-initio total energy calculations for metals

614   and semiconductors using a plane-wave basis set. Computational Materials Science, 6,

615   15-50.

616 Kresse, G. and Furthmüller, J. (1996) Efficient iterative schemes for ab initio total-energy

617   calculations using a plane-wave basis set. Physical Review B, 54, 11169-11186.

618 Lager, G.A., Armbruster, T., Rotella, F.J. and Rossman, G.R. (1989) OH substitution in garnets:

619   x-ray and neutron-diffraction, infrared, and geometric-modeling studies. American

620   Mineralogist, 74, 840-851.

621 Levien, L. and Prewitt, C.T. (1981) High-pressure crystal structure and compressibility of

622   coesite. American Mineralogist, 66, 324-333.

623 Levien, L., Prewitt, C.T. and Weidner, D.J. (1980) Structure and elastic properties of quartz at

624   pressure. American Mineralogist, 65, 920-930.

625 Libowitzky, E. (1999) Correlation of O-H stretching frequencies and O-H…O hydrogen bond

626   lengths in minerals. Monatshefte für Chemie, 130, 1047-1059.

627 Li, B., Rigden, S.M., and Liebermann, R.C. (1996) Elasticity of stishovite at high pressure.

628   Physics of the Earth and Planetary Interiors, 96, 113-127.

629 Li, L., Brodholt, J. and Alfe, D. (2009) Structure and elasticity of hydrous ringwoodite: A first

630   principle investigation. Physics of the Earth and Planetary Interiors, 177, 103-115.

631 Li, L., Weidner, D.J., Brodholt, J.P. and Alfe, D. (2011) Prospecting for water in the transition

632   zone: d ln(Vs)/d ln(Vp). Physics of the Earth and Planetary Interiors, 189, 117-120.

633 Litasov, K.D., Ohtani, E., Ghosh, S., Nishihara, Y., Suzuki, A., and Funakoshi, K. (2007)

634   Thermal equation of state of superhydrous phase B to 27 GPa and 1373 K. Physics of the

635   Earth and Planetary Interiors, 164, 142-160.

636 Liu, J., Chen, G., Gwamnesia, G.D., and Lieberman, R.C. (2000) Elastic wave velocities of

637   pyrope-majorite garnets ($Py_{62}Mj_{38}$ and $Py_{50}Mj_{50}$) to 9 GPa. Physics of the Earth and

638   Planetary Interiors, 120, 153-163.

639   Liu, L., Du, J., Zhao, J., Liu, H., Gao, H. and Chen, Y. (2009) Elastic properties of hydrous

640   forsterites under high pressure: first-principle calculations. Physics of the Earth and

641   Planetary Interiors, 176, 89-97.

642   Mao, Z., Jacobsen, S.D., Jiang, F., Smyth, J.R., Holl, C.M. and Duffy, T.S. (2008) Elasticity of

643   hydrous wadsleyite to 12 GPa: implications for Earth's transition zone. Geophysical

644   Research Letters, 35, L21305.

645   Mao, Z., Jacobsen, S.D., Jiang, F., Smyth, J.R., Holl, C.M., Frost, D.J. and Duffy, T.S. (2010)

646   Velocity crossover between hydrous and anhydrous forsterite at high pressures. Earth and

647   Planetary Science Letters, 293, 250-258.

648   Matas, J., Bass, J., Ricard, Y., Mattern, E. and Bukowinski, M.S.T. (2007) On the bulk

649   composition of the lower mantle: predictions and limitations from generalized inversion

650   of radial seismic profiles. Geophysical Journal International, 170, 764-780.

651   Mei, J., Davenport, J.W. and Fernando, G.W. (1991) Analytic embedded-atom potentials for

652   fcc metals: application to liquid and solid copper. Physical Review B, 43, 4653-4658.

653   Mellini, M. and Zanazzi, P.F. (1989) Effects of pressure on the structure of lizardite-1T.

654   European Journal of Mineralogy, 1, 13-19.

655   Mookherjee, M. and Karato, S. (2010) Solubility of water in pyrope-rich garnet at high pressures

656   and temperature. Geophysical Research Letters, 37, L03310.

657   Nobes, R.H., Akhmatskaya, E.V., Milman, V., White, J.A., Winkler, B., and Pickard, C.J. (2000)

658   An ab initio study of hydrogarnets. American Mineralogist, 85, 1706-1715.

659   Nakatsuka, A., Yoshiasa, A., Yamanaka, T., Ohtaka, O., Katsura, T. and Ito, E. (1999)

660   Symmetry change of majorite solid-solution in the system $Mg_3Al_2Si_3O_{12}$-$MgSiO_3$.

661   American Mineralogist, 84, 1135-1143.

662 Pacalo, R.E.G. and Weidner, D.J. (1996) Elasticity of superhydrous B. Physics and Chemistry of

663   Minerals, 23, 520-525.

664 Pacalo, R.E.G. and Weidner, D.J. (1997) Elasticity of majorite, $MgSiO_3$ tetragonal garnet.

665   Physics of the Earth and Planetary Interiors, 99, 145-154.

666 Panero, W.R. (2006) Aluminum incorporation in stishovite. Geophysical Research Letters, 33,

667   L20317.

668 Panero, W.R. (2010) First principles determination of the structure and elasticity of hydrous

669   ringwoodite. Journal of Geophysical Research, 115, B03203.

670 Panero, W.R., Smyth, J.R., Pigott, J.S., Liu, Z. and Frost, D.J. (2013) Hydrous ringwoodite to 5

671   K and 35 GPa: multiple hydrogen bonding sites resolved with FTIR spectroscopy.

672   American Mineralogist, 98, 637-642.

673 Pauling, L. (1980) The nature of silicon-oxygen bonds. American Mineralogist, 65, 321-323

674 Pearson, D.G., Brenker, F.E., Nestola, F., McNeill, J., Nasdala, L., Hutchison, M.T., Matveev,

675   S., Mather, K., Silversmit, G., Schmitz, S., Vekemans, B. and Vincze, L. (2014) Hydrous

676   mantle transition zone indicated by ringwoodite included within diamond. Nature, 507,

677   221-229.

678 Perdew, J.P. (1991) Unified theory of exchange and correlation beyond the local density

679   approximation, In P. Ziesche and H. Eschrig, Eds., Electronic Structure of Solids '91, p.

680   11-20, Akademie Verlag, Berlin.

681 Purton, J., Jones, R., Heggie, M., Öberg, S., and Catlow, C.R.A. (1992) LDF pseudopotential

682   calculations of the alpha-quartz structure and hydrogarnet defect, Physics and Chemistry

683   of Minerals, 18, 389-392

684 Ross, N.L., Shu, J.-F., Hazen, R.M. and Gasparik, T. (1990) High-pressure crystal chemistry of

685   stishovite. American Mineralogist, 75, 739-747.

686   Rossman, G.R. and Aines, R.D. (1991) The hydrous components in garnets: grossular-

687   hydrogrossular. American Mineralogist, 76, 1153-1164.

688   Saul, P., Catlow, C.R.A., and Kendrick, J. (1985) Theoretical studies of protons in sodium

689   hydroxide. Philosophical Magazine B, 51, 107-117.

690   Schröder, K.-P., Sauer, J., Leslie, M., Catlow, C.R.A. and Thomas, J.M. (1992) Bridging

691   hydroxyl-groups in zeolitic catalysts: a computer simulation of their structure,

692   vibrational properties and acidity in protonated faujasites (H-Y zeolites). Chemical

693   Physics Letters, 88, 320-325.

694   Sinogeikin, S.V., Bass, J.D., O'Neill, B., and Gasparik, T. (1997) Elasticity of tetragonal end-

695   member majorite and solid solutions in the system $Mg_4Si_4O_{12}$-$Mg_3Al_2Si_3O_{12}$. Physics and

696   Chemistry of Minerals, 24, 115-121.

697   Sinogeikin, S.V., Bass, J.D., Kavner, A., and Jeanloz, R. (1997) Elasticity of natural majorite and

698   ringwoodite from the Catherwood meteorite. Geophysical Research Letters, 24, 3265-

699   3268.

700   Sinogeiken, S.V., and Bass, J.D. (2000) Single-crystal elasticity of pyrope and MgO to 20 GPa

701   by Brillouin scattering in the diamond cell. Physics of the Earth and Planetary Interiors,

702   120, 43-62.

703   Sinogeikin, S.V. and Bass, J.D. (2002) Elasticity of majorite and a majorite-pyrope solid

704   solution to high pressure: implications for the transition zone. Geophysical Research

705   Letters, 29, 1017.

706   Smyth, J.R. and Jacobsen, S.D. (2006) Nominally Anhydrous Minerals and Earth's Deep Water

707   Cycle. In S.D. Jacobsen and S. van der Lee, Eds., Earth's Deep Water Cycle, 168, p. 1-

708   11, Geophysical Monograph Series, American Geophysical Union, Washingtion, D.C.

709 Smyth, J.R., Holl, C.M., Frost, D.J. and Jacobsen, S.D. (2004) High pressure crystal chemistry of

710   hydrous ringwoodite and water in the Earth's interior. Physics of the Earth and Planetary

711   Interiors, 143-144, 271-278.

712 Stachl, T. (2001) Diamonds from the asthensosphere and the transition zone. European Journal

713   of Mineralogy, 13, 883-892.

714 Thomas, S.-M., Bina, C.R., Jacobsen, S.D. and Goncharov, A.F. (2012) Radiative heat transfer

715   in a hydrous mantle transition zone. Earth and Planetary Science Letters, 357-358, 130-

716   136.

717 Tsuchiya, J. and Tsuchiya, T. (2009) First principles investigation of the structural and elastic

718   properties of hydrous wadsleyite under pressure. Journal of Geophysical Research, 114,

719   B02206.

720 Vinograd, V.L., Winkler, B., Putnis, A., Kroll, H., Milman, V., Gale, J.D. and Fabrichnaya, O.B.

721   (2006) Thermodynamics of pyrope-majorite, $Mg_3Al_2Si_3O_{12}$-$Mg_4Si_4O_{12}$, solid solution

722   from atomistic model calculations. Molecular Simulation, 32, 85-99.

723 Walker, A.M., Demouchy, S. and Wright, K. (2006) Computer modelling of the energies and

724   vibrational properties of hydroxyl groups in alpha- and beta-Mg_2SiO_4. European Journal

725   of Mineralogy, 18, 529-543.

726 Wang, Z., Wang, H., and Cates, M.E. (2001) Effective elastic properties of solid clays.

727   Geophysics, 66, 428-440.

728 Wang, J., Sinogeikin, S.V., Inoue, T. and Bass, J.D. (2003) Elastic properties of hydrous

729   ringwoodite. American Mineralogist, 88, 1608-1611.

730 Weidner, D.J., and Carleton, H.R. (1977) Elasticity of coesite. Journal of Geophysical Research,

731   82, 1334-1346.

732 Williams, Q. and Hemley, R.J. (2001) Hydrogen in the deep earth. Annual Review of Earth and

733   Planetary Sciences, 29, 365-418.

734 Withers, A.C., Wood, B.J. and Carroll, M.R. (1998) The OH content of pyrope at high pressure.

735   Chemical Geology, 147, 161-171.

736 Wright, K. (2006) Atomistic models of OH defects in nominally anhydrous minerals. Water in

737   Nominally Anhydrous Minerals, In H. Keppler and J.R. Smyth, Eds., Water in Nominally

738   Anhydrous Minerals, 62, p. 67-83, Reviews in Mineralogy and Geochemistry,

739   Mineralogical Society of America, Chantilly, Virginia.

740 Wright, K. and Catlow, C.R.A. (1994) A computer simulation study of (OH) defects in

741   olivine. Physics and Chemistry of Minerals, 20, 515-518.

742 Wright, K., Freer, R. and Catlow, C.R.A. (1994) The energetics and structure of the

743   hydrogarnet defect in grossular: a computer simulation study. Physics and Chemistry of

744   Minerals, 20, 500-503.

745 Xia, X., Weidner, D.J., and Zhao, H. (1998) Equation of state of brucite: single-crystal Brillouin

746   spectroscopy study and polycrystalline pressure-volume-temperature measurement.

747   American Mineralogist, 83, 68-74.

748 Xu, L., Mei, S., Dixon, N., Jin, Z., Suzuki, A.M. and Kohlstedt, D.L. (2013) Effect of water on

749   rheological properties of garnet at high temperatures and pressures. Earth and Planetary

750   Science Letters, 379, 158-165.

751 Yagi, T., Uchiyama, Y., Akaogi, M., and Ito., E. (1992) Isothermal compression curve of

752   $MgSiO_3$ tetragonal garnet. Physics of the Earth and Planetary Interiors, 74, 1-7.

753 Zhang, F. and Wright, K. (2010) Coupled (H^+, M^{3+}) substitutions in forsterite. Geochimica et

754   Cosmochimica Acta, 74, 5958-5965.

755 Zhang, F., and Wright, K. (2012) Coupled (Li^+, Al^{3+}) substitutions in hydrous forsterite.

756   American Mineralogist, 97, 425-429.

757 Zou, Y., Irifune, T., Gréaux, S., Whitaker, M.L., Shinmei, T., Ohfuji, H., Negishi, R., and Higo,

758   Y. (2012) Elasticity and sound velocities of polycrystalline $Mg_3Al_2(SiO_4)_3$ garnet up to

759   20 GPa and 1700 K. Journal of Applied Physics, 112, 014910.

760

761   **Figure Captions**

762   **Figure 1.** Crystal structure of defect-free $MgSiO_3$ tetragonal garnet optimized using

763   force fields. The two octahedral sites are occupied by Si (pink) and Mg (blue). Mg atoms (light

764   blue) occupy two unique interstitial sites. Three unique tetrahedral sites are occupied by Si (red).

765   **Figure 2.** Enthalpy associated with protonating each oxygen site calculated using the

766   force field approach.

767   **Figure 3.** OH-defect structures in $MgSiO_3$ majorite optimized using force fields.

768   Hydrogen atoms are light blue and the oxygen atoms are color-coded according to atomic site

769   where O1=red, O2=light green, O3=dark blue, O4=yellow, O5=dark green, O6=purple. (a)

770    $[V_{Mg2} + 2OH_{O5}]^X$ (b) $[V_{Mg3} + 2OH_{O5}]^X$ (c) $[V_{Si4} + 2OH_{O2} + 2OH_{O3}]^X$ (d) "Hydrogarnet"-type $[V_{Si2}$

771    $+ 4OH_{O6}]^X$.

772   **Figure 4.** Enthalpies of reactions 6 (Al-free) and 7 (Al_2O_3 = 0.4 wt%) calculated as a

773   function of pressure using the force field approach. Negative values of the enthalpy correspond

774   to the hydrogarnet defect being favored.

775   **Figure 5.** Calculated enthalpies (reactions 8 and 9) using force fields for hydrogen

776   incorporation via (a) Mg and (b) Si vacancies in the presence of a coupled-substitution of Al for

777   ^{IV}Si or ^{VI}Si and ^{VI}Mg as a function of pressure. Open symbols represent calculations using a 2 x

778   2 x 2 supercell, and the filled symbols represent calculations using the conventional tetragonal

779   unit cell.

780   **Figure 6.** (a) V_p and (b) V_s for Al-free anhydrous and hydrous majorite calculated as a

781   function of pressure using force fields.

782   **Figure 7.** The force field calculated majorite $dlnV_s/dlnV_p$ due to compositional changes

783   resulting from OH incorporation compared to experimental and computational results for the

784　olivine polymorphs (Li et al., 2011). The results from this study are shown by red squares $([V_{\text{Mg3}}$

785　$+2\text{OH}_{\text{O5}}]^{X}$, C_{water} = 1400 ppm$)$, blue triangles $([V_{\text{Si2}}+4\text{OH}_{\text{O6}}]^{X}$, C_{water} = 1400 ppm$)$, light blue,

786　open squares $(V_{\text{Si2}}+4\text{OH}_{\text{O6}}]^{X}$, C_{water} = 1.13 wt%) and light blue triangles $(V_{\text{Si2}}+4\text{OH}_{\text{O6}}]^{X}$, C_{water}

787　= 1.13 wt%, C_{Al2O3} = 3.2 wt%).   Experimental results (filled black symbols) for forsterite

788　(square) (Mao et al. 2010), wadsleyite (triangle) (Mao et al. 2008), and ringwoodite (circle)

789　(Inoue et al. 1998; Wang et al. 2003) are shown. Additional computational results (black open

790　symbols and dashed lines) are also shown for forsterite (triangles) (Tsuchiya and Tsuchiya

791　2009), wadsleyite (circles) (Liu et al. 2009), and ringwoodite (squares and dashed line without

792　symbols) (Panero 2010; Li et al. 2009), respectively. For comparison, the thermal $d\ln V_s/d\ln V_p$

793　for ringwoodite (Li et al. 2011) is shown by the orange dotted line.

794

Tables

Table 1. Interatomic potential parameters and ionic charges.

Species	q (e)
Mg(core)	1.7
Si(core)	3.4
Al(core)	2.55
O(core)	0.746527
O(shell)	-2.446527
O_H(core)[a]	-1.2
H(core)	0.35

Interaction			
Buckingham	A (eV)	ρ (Å)	C (eV $\cdot$ Å^6)
Mg(core) – O (shell)	1432.8544	0.277265	0.0
Si(core) – O (shell)	1073.4668	0.298398	0.0
Al(core) – O (shell)	1262.2081	0.28637	0.0
Mg(core) – O_H(core)	1015.8587	0.277265	0.0
Si(core) – O_H(core)	761.06168	0.298398	0.0
Al(core) – O_H(core)	894.87465	0.28637	0.0
O(shell) – O(shell)	598.8996	0.314947	26.89746
O(shell) – O_H(core)	598.8996	0.314947	26.89746
O_H (core) – O_H(core)	598.8996	0.314947	26.89746
H(core) – O(shell)	191.6667	0.25	0.0
H(core) – O_H(core)	191.6667	0.25	0.0

Morse	D_e (eV)	a (Å^{-1})	r_0 (Å)
H(core) – O_H(core)	7.0525	2.1986	0.94285

Spring	k_2 (eV/Å^2)	k_4 (eV/Å^4)
O(core) – O(shell)	56.5598	10000.0

Three-body	k_θ (eV/rad^2)	θ (degrees)
O – ^{IV}Si – O	0.77664	109.47
O – ^{VI}Si – O	2.2955	90.0
O – ^{IV}Al – O	1.2883	109.47
O – ^{VI}Al – O	1.8807	90.0

798   **Table 2.**   Calculated structural parameters for tetragonal $MgSiO_3$ majorite compared to

799   published experimental and computational data.

Cell parameters	XRD[a]	SLEC This Study	% difference	SLEC[b]	DFT-GGA This Study	DFT-GGA[b]
			$P = 0$ GPa			
a (Å)	11.501(1)	11.506	0.04	11.494	11.638	11.670
c (Å)	11.480(2)	11.416	-0.56	11.392	11.528	11.561
c/a	0.9982(2)	0.9922	-0.60	0.9912	0.9905	0.9907
V(Å^3)	1518.6(4)	1511.27	-0.48	1505.04	1561.34	1574.47
			$P = 10$ GPa			
a (Å)	11.315	11.307	-0.07	–	–	–
c (Å)	11.214	11.211	-0.03	–	–	–
c/a	0.9911	0.9915	0.04	–	–	–
V(Å^3)	1435.7	1433.33	-0.17	–	–	–
			$P = 20$ GPa			
a (Å)	–	11.144	–	–	11.251	–
c (Å)	–	11.048	–	–	11.115	–
c/a	–	0.9913	–	–	0.9879	–
V(Å^3)	–	1372.05	–	–	1407.06	–

[a]Ambient condition (Angel et al. 1989) and P = 9.72 GPa experiments (Yagi et al. 1992) and ; [b]CASTEP
(Vinograd et al. 2006)

800

801 **Table 3.** Elastic constants, bulk (K_s) and shear (μ) moduli of tetragonal majorite garnet

802 ($MgSiO_3$).

Elastic constants	Experimental (GPa)	SLEC This study (GPa)	SLEC[b] (GPa)
	P = 0 GPa		
C_{11}	[a]286.4(13)	296.52	295.10
C_{33}	[a]280.1(18)	296.14	–
C_{44}	[a]85.0(7)	86.05	85.23
C_{66}	[a]93.2(11)	94.14	93.66
C_{12}	[a]83.0(29)	112.5	112.7
C_{23}	[a]104.9(24)	102.42	–
C_{16}	[a]1.4(13)	14.30	14.72
	P = 10 GPa		
C_{11}	–	347.04	–
C_{33}	–	350.51	–
C_{44}	–	92.99	–
C_{66}	–	103.66	–
C_{12}	–	141.27	–
C_{23}	–	132.47	–
C_{16}	–	21.55	–
	P = 20 GPa		
C_{11}	–	392.16	–
C_{33}	–	398.69	–
C_{44}	–	97.96	–
C_{66}	–	109.86	–
C_{12}	–	170.97	–
C_{23}	–	164.06	–
C_{16}	–	26.36	–
Isotropic properties			
	P = 0 GPa		
K_s	[a]159.8(44), [c]167.3(33) [d]164.4(5), [e]170(5), [f]166(3) [g]166(5), [h]164(4)	169.3	170.14
μ	[a]89.7(6), [c]88.3(18), [d]94.9(2) [e]89(1), [f]85(2), [g]88(2), [h]87(2)	90.8	–
	P = 10 GPa		
K_s	[b]210(4)	206.3	–
μ	[b]103(2)	99.4	–
	P = 20 GPa		
K_s	–	242.4	–
μ	–	105.3	–

803 [a]Ambient condition experiments, Mj_{100} (Pacalo and Weidner 1997); [b]Vinograd et al. (2006); [c]Mj_{100} (Gwamnesia et
804 al. 1998); [d]pyrolite minus olivine composition (Irifune et al. 2008); [e]$Mj_{50}Py_{50}$ (Liu et al. 2000); [f]Mj_{100} (Sinogeikin
805 and Bass 2002); [g]Mj_{100} (Sinogeikin et al. 1997a); [h]natural Catherwood meteorite sample (Sinogeikin et al. 1997b)

806 **Table 4.** Calculated vacancy formation energy and crystalline lattice energies from force fields

807 implemented in GULP.

Defect	Formation Enthalpy (eV)	
Unbound vacancies	0 GPa	25 GPa
V_{Mg1}''	18.89	19.50
V_{Mg2}''	18.77	19.38
V_{Mg3}''	19.43	20.26
V_{Si1}''''	76.61	78.89
V_{Si2}''''	70.07	71.95
V_{Si3}''''	73.39	75.84
V_{Si4}''''	72.56	74.36
$V_{O1}^{\cdot\cdot}$	17.06	16.78
$V_{O2}^{\cdot\cdot}$	16.69	16.92
$V_{O3}^{\cdot\cdot}$	15.93	15.56
$V_{O4}^{\cdot\cdot}$	15.96	15.54
$V_{O5}^{\cdot\cdot}$	15.95	15.56
$V_{O6}^{\cdot\cdot}$	17.08	17.31
Bound vacancies		
$[V_{Mg1} + V_{O1}]^x$	35.86	36.34
$[V_{Mg1} + V_{O2}]^x$	35.44	36.32
$[V_{Mg1} + V_{O3}]^x$	34.97	34.99
$[V_{Mg1} + V_{O4}]^x$	35.87	35.03
$[V_{Mg1} + V_{O5}]^x$	34.90	35.01
$[V_{Mg1} + V_{O6}]^x$	36.15	37.07
$[V_{Mg2} + V_{O1}]^x$	35.20	35.24
$[V_{Mg2} + V_{O2}]^x$	35.04	35.24
$[V_{Mg2} + V_{O5}]^x$	34.66	34.68
$[V_{Mg2} + V_{O6}]^x$	35.47	36.59
$[V_{Mg3} + V_{O1}]^x$	35.69	35.88
$[V_{Mg3} + V_{O4}]^x$	36.40	34.81
$[V_{Mg3} + V_{O5}]^x$	34.67	35.04
Phase		
MgO	-30.18	-27.44
α-Quartz	-95.35	-
Stishovite	-	-91.06

808

809   **Table 5.** Enthalpies calculated from first principles at the DFT-GGA level of theory.

	0 GPa	20 GPa
Enthalpy (eV)		
MgO[a]	-12.01	-9.71
SiO_2, α-quartz[a]	-23.98	–
SiO_2, stishovite[a]	–	-20.55
Majorite[b]	-1147.67	-963.27
Defect Formation Enthalpy (eV/H)		
$V_{Mg3}'' + 2(OH_{O5}^{.})$	-0.51	-0.62
$V_{Si2}'''' + 4(OH_{O6}^{.})$	-1.37	-1.16
Reaction enthalpy (eV/H)		
Reaction 6	-0.85	-0.82

810   [a]1 formula unit; [b]Full unit cell (8 formula units)